RSC Advances

This is an *Accepted Manuscript*, which has been through the Royal Society of Chemistry peer review process and has been accepted for publication.

Accepted Manuscripts are published online shortly after acceptance, before technical editing, formatting and proof reading. Using this free service, authors can make their results available to the community, in citable form, before we publish the edited article. This *Accepted Manuscript* will be replaced by the edited, formatted and paginated article as soon as this is available.

You can find more information about *Accepted Manuscripts* in the **Information for Authors**.

ROYAL SOCIETY
OF **CHEMISTRY**

www.rsc.org/advances

RSC Advances

ARTICLE

Hydrothermally Synthesized Graphene and Fe₃O₄ Nanocomposites for High Performance Capacitive Deionization

Haibo Li,[a] Zhiyi Leong,[a] Wenhui Shi,[a] Jun Zhang,[b] Chen Tupei[b] and Yang Hui Ying[a]*

Capacitive deionization (CDI) devices with low energy consumption and high salt removal efficiencies have attracted much attention. Recently, graphene has been proved to be one of the most promising materials for CDI electrodes. However, pristine graphene is far from desirable due to its low removal efficiency and unavoidable decays in performance. In this study, a reduced graphene oxide/Fe₃O₄ nanoparticle (RGO@Fe₃O₄) hybrid is proposed and synthesized via a hydrothermal approach for enhanced CDI. Electrochemical analysis of this nanocomposite material has revealed typical an electrical double layer capacitive behaviour and an improved specific capacitance. Furthermore, the electrosorption capacity and current efficiency of RGO@Fe₃O₄ were found to be nearly two folds higher than that of RGO. This huge improvement is attributed to the hydroxylation of the Fe₃O₄ surface. In addition, the maximum electrosorption capacity predicted from the Langmuir isotherm was ~ 8.33 and ~ 4.63 mg/g, corresponding to RGO@Fe₃O₄ and RGO electrode, respectively.

1. Introduction

In the past decade, capacitive deionization (CDI) has emerged as one of the most promising techniques to produce portable water from saline water. It has attracted much attention due to its low driving energy, high removal efficiency, high water recovery rate, cost effectiveness and low environmental impact [1-5]. In a typical CDI process, charged species in solution are electrostatically attracted to the surface of oppositely charged electrodes to form electrical double layers (EDL) and this generates a diluted solution. Since the desalination performance of CDI is dependent on electrodes to provide the vacancies to accommodate ions, the physicochemical characteristics associated with electrodes are significant. In CDI research, porous carbon based electrodes using mesoporous carbon [6], carbon nanotubes [7], carbon aerogels [8] and graphene [9] have been employed as electrode materials for achieving high performance in CDI due to their large surface areas, mild pore size distribution and tuneable electrical conductivities.

Among the aforementioned carbon materials, graphene possesses the highest theoretical surface area of ~2600 m²/g. Its high surface area coupled with the ease of mass production through wet synthesis approach makes it an attractive

material for investigation. However, graphene sheets are prone to agglomeration during the reduction process of graphene oxide (GO) [10] and this leads to uncontrollable pore size distribution and low surface areas. Consequently, it decreases the EDL capacitance of electrodes and deteriorates the CDI performance. To circumvent this problem, a variety of methods have been developed to suppress the restacking of graphene sheets. For example, graphene/mesoporous carbon composites were fabricated to form a mesoporous structure [11]. This composite showed an electrosorption capacity of 0.73 mg/g with an applied potential of 2.0 V in a 40 mg/L NaCl solution. In a separate study, carbon nanotubes (CNT) were synthesized with graphene to form composites with increased specific surface areas [12]. These composites exhibit an improved electrosorption capacity of 1.41 mg/g at 2.0 V in a 25 mg/L NaCl solution. In addition, resorcinol-formaldehyde (RF) resins were coupled with graphene to alleviate the aggregation of graphene sheets [13]. The prepared RGO@RF electrode showed a promising electrosorption capacity of 3.47 mg/g at a potential of 2.0 V in a 40 mg/L NaCl solution. Hence, it has been shown that the functionalization of graphene can improve the overall CDI performance.

Despite these advances, a rational design is needed to fully utilize the high surface area and further improve the CDI performance. To that end, many researchers have embarked on the synthesis of unique graphene architectures with remarkable qualities. One example would be three-dimensional (3D) graphene. This type of graphene has an interconnected macroporous structure which is beneficial in buffering ions and reducing the diffusion distance from an external electrolyte to the internal surfaces. Following this

[a.] Pillar of Engineering Product Development, Singapore University of Technology and Design, 8 Somapah Road, Singapore 487372. E-mail: yanghuiying@sutd.edu.sg
[b.] School of Electrical and Electronics Engineering, Nanyang Technological University, Singapore 639798

direction, graphene materials with open structures were developed. These include 3D macroporous graphene [14], 3D sponge-template graphene [15,16] as well as its composite with carbon nanotubes [17,18]. 3D graphene was synthesized by Zhang et.al. via a versatile template-directed method which resulted in a high surface area of 339 m^2/g with an average pore diameter of 4 nm [14]. It showed an electrosorption capacity of 3.9 mg/g with a potential of 1.6 V in a 52 mg/L NaCl solution. A downside to this strategy is that the synthesis process is relatively complicated, time-consuming, and costly. More importantly, the calculated theoretical electrosorption capacity of such graphene structures is limited.

An inherent advantage graphene sheets have over amorphous or 1D carbon materials is its ability to easily self-assemble into 3D networks [19]. This not only creates a large number of open pores that are accessible to NaCl molecules but also enables the growth and anchoring of functional organic/inorganic materials with high loading amounts [20, 21]. In particular, the incorporation of metal oxides will significantly improve the capacitance of graphene-based materials [22]. Fe_3O_4 for example, is environmentally benign, chemically stable and has high pseudocapactiance through redox reactions. Potentially, Fe_3O_4 is a choice material for the synthesis of graphene/metal oxide nanocomposites for energy storage and related technologies [23].

In this work, reduced graphene oxide and Fe_3O_4 (RGO@Fe_3O_4) hybrids were prepared by a facile hydrothermal method and fabricated as electrodes for symmetrical CDI. The cyclic voltammetry (CV) curve of RGO@Fe_3O_4 exhibits a typical electrical double layer capacitive behaviour. Compared to RGO, the enhanced capacitance of RGO@Fe_3O_4 may arise from an exchange activity between the hydrated Fe_3O_4 and Na^+. Subsequently, the electrosorption performance of RGO@Fe_3O_4 and RGO were comparatively investigated. It is found that the removal capacity, electrosorption rate constant and charge efficiency of RGO@Fe_3O_4 is nearly twice as high as that of RGO. Additionally, the maximum removal capacity of RGO@Fe_3O_4 is predicted by the Langmuir model, which shows a high value of $\sim$ 8.33 mg/g.

2. Experimental

2.1 Synthesis of RGO@Fe_3O_4

Graphene oxide (GO) was prepared according to a modified hummers' method which has been documented in our previous studies [24]. A typical synthesis procedure for synthesizing RGO@Fe_3O_4 is as follows: 0.025 g GO is first dispersed by ultrasonication in 7 mL of ethylene glycol for 1 hour to obtain solution A. Next, 0.1 g of $Fe(NO_3)_3 \cdot 9H_2O$ and 0.051 g KOH were separately dissolved in 15 mL ethylene glycol under vigorous stirring for 10 minutes to get solution B. Subsequently. Solution A and B were loaded in a Teflon lined autoclave, which was then filled with ethylene glycol up to 80% of the total volume. The autoclave was sealed and maintained at a certain temperature which was controlled from 200 °C to 250 °C for 24 h. Finally, it was cooled down to room temperature naturally. The products were washed

several times with deionized water and absolute ethanol to remove any impurities and dried at 60 °C for 6 h to obtain the final product.

2.2 Characterization

The surface morphologies and energy dispersive spectroscopy (EDS) spectrum of the samples were characterized by a field emission scanning electron microscope (FESEM, JEOL JSM-7600F) and a transmission electron microscope (TEM, JEOL JEM-2100F). Next, the Raman measurements were carried out using a WITec alpha 300 confocal Raman microscope equipped with a 532 nm solid-state laser for excitation. The Brunauer–Emmett–Teller (BET) specific surface area were deduced from the automatic high-resolution physisorption (micropore/mesopore) analyzer using an Autosorb-iQ-MP-XR System (Quantachrome, USA), and the pore size distribution was derived from the adsorption branches of the isotherms using the Barrett–Joyner–Halenda (BJH) method. The crystalline nature of the samples was investigated using an X-ray diffractometer (Bruker, D8 Advance-Eco) equipped with a Kα radiation ($\lambda \approx 1.54$ Å) source. Thermogravimetric analysis (TGA) was carried out using Shimadzu DTG-60 under compressed air flow gas at a rate of 5 °C/min. X-Ray photoelectron spectroscopy (XPS, Thermo ESCALAC250Xi) spectra was collected on a monochromatized Al Ka X-ray source (1486.6 eV).

2.3 Electrochemical test

The RGO@Fe_3O_4 electrodes were fabricated as follows: RGO@Fe_3O_4, carbon black and polyvinylidene fluoride were mixed in a mass ratio of 80:10:10 and dispersed in ethanol with the addition of a few drops of dimethylformamide. The resulting mixture was coated onto the graphite paper with a spatula, followed by drying at 60°C for 12 h. The electrochemical measurements were performed in a typical three-electrode setup composed of either RGO or RGO@Fe_3O_4 as working electrodes, Pt foil as the counter electrode and a saturated calomel electrode (SCE) as the reference electrode. CV measurements were performed at various scan rates from 1 to 100 mV/s on an electrochemical workstation (VMP3, Bio-logic, France) in 1 M NaCl solutions.

2.4 CDI experiment

The desalination performance of both RGO and RGO@Fe_3O_4 was investigated by conducting batch-mode electrosorption experiments using a continuously recycling system which has been described in our previous work [25, 26]. The total mass of electrodes is 0.07 g. At the start of each experiment, an analytically pure NaCl solution of 40 mL was prepared. The concentration of NaCl solution was varied from 50 to 500 mg/L whereas the applied direct voltage varied from 1.0 to 1.6 V. Other experimental parameters which remain constant were the flow rate (30 mL/min) and solution temperature (298K). The relationship between conductivity and concentration was obtained according to a calibration table made prior to the experiment. The concentration variation was continuously monitored and measured at the outlet of the unit cell using an

ion conductivity meter (DSJ 308F, LeiCi, Shanghai). The electrosorption capacity (Γ, mg/g) can be calculated as:

$$\Gamma = (C_f - C_0) \times V / M \qquad (1)$$

Where C_0 and C_f are the initial and final NaCl concentrations (mg/L), respectively, V is the volume of NaCl solution (L) and m is the total mass of the electrodes (g).

3. Results and Discussion

Figure 1(a) and (b) show the SEM image of RGO and RGO@Fe$_3$O$_4$. It clearly reveals that Fe$_3$O$_4$ nanoparticles (NPs) have fully incorporated onto RGO layers without aggregation. The EDS mapping analysis on C, Fe and O shown in Figure 1(e) confirm the chemical composition for the RGO@Fe$_3$O$_4$ hybrid electrode. The detailed nanostructures of the hybrid RGO@Fe$_3$O$_4$ is further investigated by high-resolution TEM (HRTEM) imaging. As shown in Figure 1(c) and (d), a large amount of Fe$_3$O$_4$ NPs with diameters ranging from 10 to 200 nm is uniformly distributed on the RGO layers. Moreover, an enlarged image containing a Fe$_3$O$_4$ NP is given in inset of Figure 1(c). It can be seen that the Fe$_3$O$_4$ NP is tightly wrapped with RGO sheets. This surface decoration by RGO promotes an interconnected architecture between individual clusters of Fe$_3$O$_4$ nanocrystals to form a 3D network structure, thus facilitating ion transportation between Fe$_3$O$_4$ and RGO sheets. Further, the inset of Figure 1(c) shows the lattice fringes of Fe$_3$O$_4$ and reveals an interspacing of ~0.296 nm which corresponds to the (311) plane of Fe$_3$O$_4$.
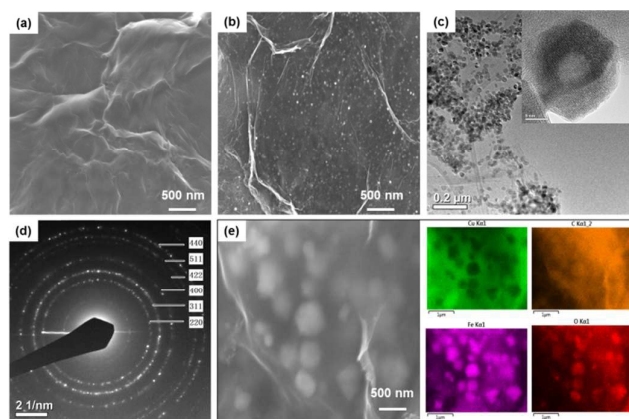

Figure 1 SEM image of RGO (a) and RGO@Fe$_3$O$_4$ (b), (c) TEM image of RGO@Fe$_3$O$_4$ (inset is the TEM image of a Fe$_3$O$_4$ NP) and (d) SAED pattern, (e) the SEM image and EDX mapping of (b) Cu, (c) C, (d) Fe and (e) O for RGO@Fe$_3$O$_4$ (note that the Cu is from the substrate).

The selected area electron diffraction (SAED) pattern shows a face centered cubic crystal structure of Fe$_3$O$_4$, which is confirmed by the XRD pattern shown in Figure 2(a) as well. Figure 2(b) is the Raman spectra of RGO@Fe$_3$O$_4$. It shows 4 typical peaks of the Fe-O stretching vibration which indicates successful synthesis of RGO@Fe$_3$O$_4$ nanocomposites. The Raman bands at 218.8 and 491.3 cm^{-1} are attributed to the scattering of A$_{1g}$ mode of Fe$_3$O$_4$, whereas the bands at 283,

394.1 and 593.4 cm^{-1} are attributed to the scattering of E$_g$ mode of Fe$_3$O$_4$. Besides that, the characteristic D and G bands of the RGO@Fe$_3$O$_4$ hybrid were observed at 1344 and 1586 cm^{-1} respectively. The D band is associated with disordered samples or graphene edges, while the G band is the result of first-order scattering of the E$_{2g}$ mode of sp2 carbon domains. Both the position and intensity of D and G bands are highly susceptible to structural changes of the carbon matrix and many factors affect the position and intensity of D and G bands. These include doping effects, layer numbers, defects, strains and substrates. It is observed that the ratio of ID over IG is 1.05 which is higher than 1, thus confirming the reduction of GO to RGO. The N$_2$ adsorption-desorption isotherm is presented in Figure 2(c). It shows cross curves between type-I and type-IV curves, demonstrating the presence of micro/mesopores in this composite. The BET surface area of RGO@Fe$_3$O$_4$ is measured to be 150.8 m^2/g and the corresponding BJH desorption pore volume is 0.166 m^3/g. The high specific surface area is attributed to excellent dispersion of RGO and promotes the diffusion of electrolyte to the activate sites [27]. The inset in Figure 2(c) represents the pore size distribution of RGO@Fe$_3$O$_4$. A broad peak from 2 to 5 nm is observed in the curve, confirming the mesoposity of RGO@Fe$_3$O$_4$ according to the IUPAC classification. TGA was utilized to determine the amount of RGO within the hybrid. Figure 2(d) shows the TGA graph for the RGO@Fe$_3$O$_4$. From this figure, it can be seen that the burning of RGO ranges approximately from 150 °C to 420 °C. The residual remains after 420 °C is due to the presence of Fe$_3$O$_4$ NPs. Thus, the weight ratio of RGO over Fe$_3$O$_4$ NPs is ~1:1.5. It should be mentioned that low amount of RGO in the hybrid would result in low specific surface area which is not desirable in CDI experiment.
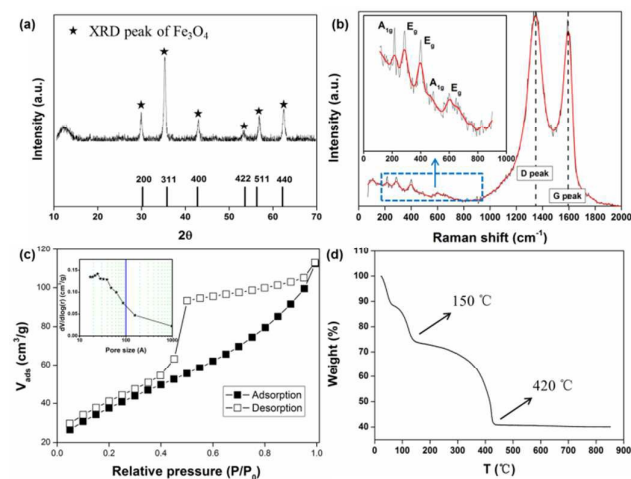

Figure 2 The XRD (a), Raman (b), N$_2$ adsorption-desorption isotherm (c) and (d) TGA curve of RGO@Fe$_3$O$_4$ (inset in (b) is magnified selected area while inset in (c) is corresponding pore size distribution).

The extent of the residual oxygen on the graphene sheet during hydrothermal treatment is examined by XPS. Fig. 3(a) shows the XPS spectrum of C1s for Fe$_3$O$_4$-RGO which could be

deconvoluted into three peaks (colored lines) with different carbon ratios: sp2 bonded carbon at 284.5 eV (C–C), epoxy/hydroxyls at 286.4 eV (C–O) and carbonyls at 288.4 eV (C=O). Obviously, it presents the high percentage of oxygen-containing functional groups due to incomplete reduction by hydrothermal reaction. It should be noted that XPS spectrum of O1s shows the similar results. Fig. 3(b) exhibits the Fe2p spectrum of Fe_3O_4. Clearly, due to the Spin-orbit coupling, Fe2p core level is split into $2p_{1/2}$ and $2p_{3/2}$ components. Because the binding energy of Fe^{2+} and Fe^{3+} in the $Fe2p_{3/2}$ spectrum is expected to be 709.4 eV and 710.8 eV, respectively, the asymmetric broadband centered at around 710 eV manifests the coexistence of Fe^{3+} and Fe^{2+}.
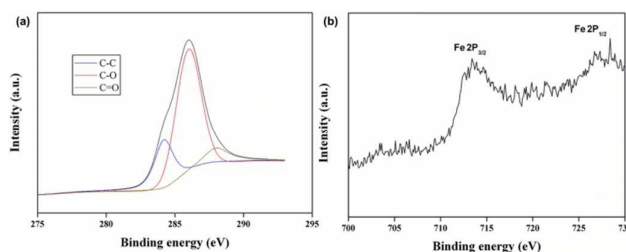

Figure 3 C1s (a) and Fe 2p (b) region in the XPS spectrum of the as-synthesized RGO@Fe_3O_4.

CV measurements were extensively employed to study the electrochemical behavior and to determine the specific capacitance of the electrodes. Figure 4(a) displays the representative CV curves of RGO/RGO@Fe_3O_4 at a scanning rate of 10 mV/s in 1 M NaCl solution while Figure 4(b) depicts the corresponding specific capacitance at scanning rates ranging from 1 to 100 mV/s. The curves of both RGO and RGO@Fe_3O_4 demonstrate an almost rectangular shape without presenting any peaks, suggesting double layer capacitive behavior. Compared to that of RGO electrode, the CV curve of RGO@Fe_3O_4 has a larger integrated CV area, implying a higher specific capacity. The improvement of the specific capacity from RGO to RGO@Fe_3O_4 is mainly ascribed to the hydroxylation of Fe_3O_4 surface [28]. Thus, diffusion and adsorption of ions become facile on the hybrid electrode. The mechanism of this process is probably as follows:
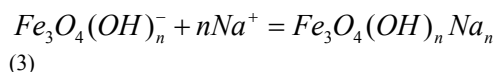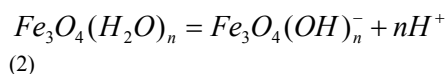
$$Fe_3O_4(H_2O)_n = Fe_3O_4(OH)_n^- + nH^+$$
(2)

$$Fe_3O_4(OH)_n^- + nNa^+ = Fe_3O_4(OH)_n Na_n$$
(3)

Figure 4(c) exhibits the electrosorption-desorption cycle of RGO@Fe_3O_4 in NaCl solution with an initial conductivity of 500 µS/cm at a voltage of 1.2 V and the inset shows the corresponding current transient. Once the electrical voltage is applied, the conductivity decreases significantly. After 30 minutes, the conductivity gradually decreases to 465 µS/cm and does not change anymore, indicating that equilibrium is reached. Then the CDI unit is shorted, resulting in a desorption process. The solution conductivity returns to its initial level and

regeneration is completed. Similarly, the current curve follows the same transient (inset). Figure 4(d) shows the conductivity and current transition (inset) of RGO@Fe_3O_4 at electrical voltages of 1.0, 1.2, 1.4 and 1.6 V respectively. Clearly, the higher voltage is, the higher salt removal capacity is.
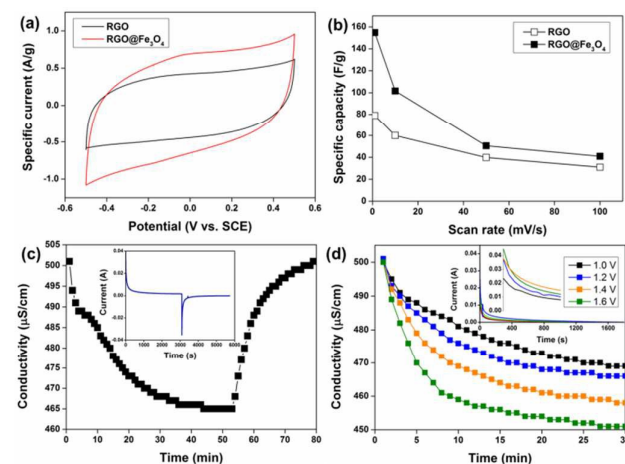

Figure 4 (a) the CV curve of RGO and RGO@Fe3O4 in 1 M NaCl solution at the scanning rate of 10 mV/s, (b) the specific capacity of RGO and RGO@Fe_3O_4 dependent on scanning rate, (c) a complete electrosorption-desorption cycle for RGO@Fe_3O_4 electrode at 1.2 V and (d) electrosorption performance of RGO@Fe_3O_4 at different electrical voltage in NaCl solution with an initial conductivity of 500 µS/cm (inset in (c) and (d) are corresponding current transient)

In order to make reasonable comparisons, the normalized removal capacity (mg/g) of the RGO/ RGO@Fe_3O_4 electrode under different cell voltages (V) is plotted in Figure 5(a). For both electrodes, an increase in electrical voltage results in higher removal capacity due to higher electrostatic force. At a certain voltage, the removal capacity of RGO@Fe_3O_4 is nearly two folds higher than RGO. The current efficiency is also calculated and shown in Figure 6(a). It is defined as:

$$\Lambda = \frac{\Gamma \times F}{58.5 \times \Sigma} \times 10^{-3}$$
(4)

where F is the Faraday constant (96485 /mol), Γ (removal capacity, mg/g) and Σ (specific charge which is obtained by integrating the current (A) with time (s), C/g). In the case of an ideal CDI process, each electron charge is fully charge-balanced by a counter ion adsorption and the transfer of an electron from one electrode to another is accompanied by the removal of precisely one salt molecule from the bulk solution. However, due to co-ions impaction caused by simultaneous adsorption, the current efficiency is often less than 1 which means that the majority of input energy is lost, leading to low energy efficiency. It can be seen from Figure 6(a) that RGO has a very low current efficiency (0.32 at 1.2 V). This implies that significant co-ions impaction had taken place before electrode charging, probably due to incomplete reduction of GO. As for RGO@Fe_3O_4 electrodes, the current efficiency is highly improved. At each certain electrical voltage, the current efficiency of RGO@Fe_3O_4 is nearly two folds higher than that of RGO, which implies less co-ions impaction had taken place.

The electrosorption rate of NaCl onto RGO@Fe$_3$O$_4$ is a crucial parameter in our investigations of the CDI process. Therefore, the pseudo-first-order model is employed and its linearized forms of equation can be expressed as:

$$\log(Q_e - Q_t) = \log Q_e - k_{ad} \times t / 2.303$$

(5)

where Q$_e$ and Q$_t$ are the amounts of the ions adsorbed (mg/g) at equilibrium and at time t (min), respectively. k$_{ad}$ (min^{-1}) is the rate constant of pseudo-first-order model. Figure 5(b) shows the experimental data at various electrical voltages as well as the fitting line using the model equation. The rate constant is obtained from the slope of the lines in Figure 5(b) and is summarized in Table 1. The kinetics of the adsorption process can be evaluated based on how close the regression coefficient (R^2 in Table 1) is to unity. From the data given in Table 1, it can be seen that the simulated lines agree well with experimental data and an increase in electrosorption rate constant is observed as the voltage is increased from 1.0 V to 1.6 V. This result is consistent with the conductivity variation observed in Figure 4(b). It is also observed that the rate constant k$_{ad}$ of RGO@Fe$_3$O$_4$ is much higher than that of RGO regardless of the applied voltage.
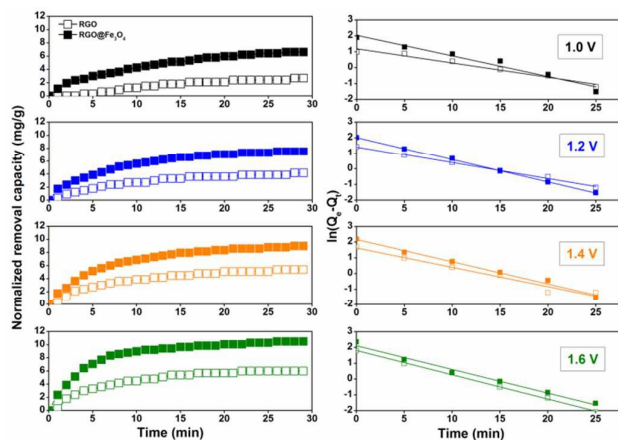

Figure 5 (a) the mass normalized salt removal capacity and (b) kinetic fitting for RGO and RGO@Fe$_3$O$_4$ at different electrical voltages.

Table 1 Parameters of the first order kinetics

	1.0 V		1.2 V	
	RGO	RGO@Fe$_3$O$_4$	RGO	RGO@Fe$_3$O$_4$
K$_{ad}$ (min^{-1})	0.2059	0.2987	0.2349	0.3289
R^2	0.9642	0.9578	0.9949	0.9992
	1.4 V		1.6 V	
	RGO	RGO@Fe$_3$O$_4$	RGO	RGO@Fe$_3$O$_4$
K$_{ad}$ (min^{-1})	0.2836	0.3258	0.3449	0.3455
R^2	0.9611	0.9871	0.9958	0.9839

The Langmuir adsorption isotherm is often employed to describe the electrosorption behavior and predict the maximum adsorption capacity of electrodes in NaCl solutions. The equation of Langmuir isotherms is shown as follows:

$$Q = \frac{Q_m K_L C}{1 + K_L C}$$

(6)

where Q$_m$ is the maximum adsorption capacity corresponding to complete monolayer coverage (mg/g), K$_L$ is the Langmuir constants, and C is the equilibrium concentration (mg/L). The experimental data and fitting line in terms of RGO@Fe$_3$O$_4$ and RGO electrode are given in Figure 6(b). All parameters involving Q$_m$, K$_L$ and R^2 (regression coefficient) are presented in Table 2. Based on the calculated the R^2, it can be seen that the Langmuir isotherm perfectly describes the electrosorption performance of both RGO@Fe$_3$O$_4$ and RGO electrodes. Correspondingly, the Langmuir isotherm predicts a higher maximum adsorption capacity, Q$_m$ for RGO@Fe$_3$O$_4$ electrodes (8.33 mg/g) than RGO (4.63 mg/g).

Complete regeneration of electrodes is essential for commercial applications of CDI. Figure 6(c) shows an experiment of 5 electrosorption-desorption cycles of RGO@Fe$_3$O$_4$ electrode which is carried out by repeating several charging (1.2 V) and discharging (0 V) processes in a NaCl solution with an initial conductivity of 500 μS/cm. It can be seen that the repeatability of electrosorption process can be realized through RGO@Fe$_3$O$_4$ electrode. Furthermore, the electrosorption capacity declination has not been observed for RGO@Fe$_3$O$_4$ even after over 30 charge-discharge cycles, implying an excellent regeneration.
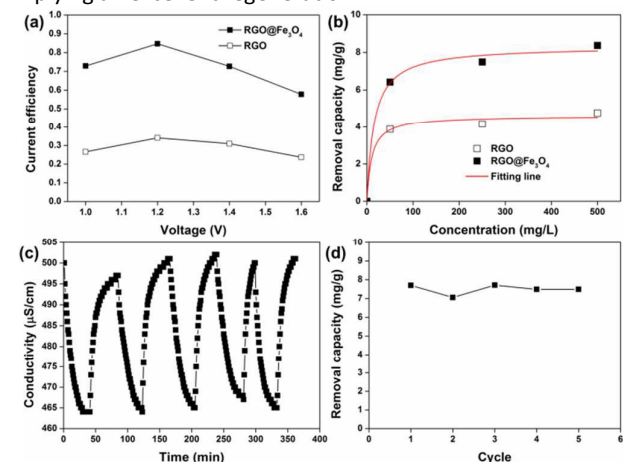

Figure 6 (a) the current efficiency of RGO and RGO@Fe$_3$O$_4$ at different voltage, (b) the Langmuir isotherm of RGO and RGO@Fe$_3$O$_4$, (c) the regeneration curve of RGO@Fe$_3$O$_4$ in five cycles, (d) the salt removal capacity with respect to cycles.

Table 2 Parameters of the Langmuir isotherm.

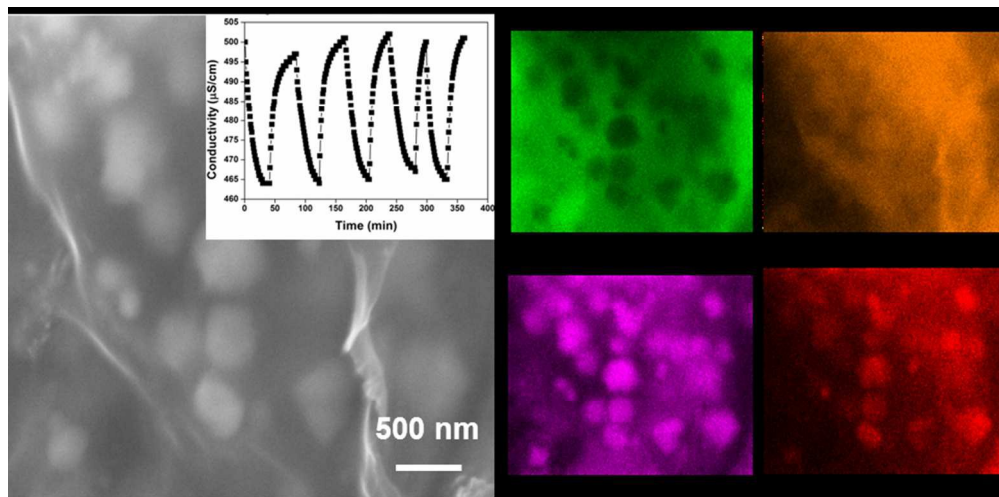|	Qm (mg/g)	K_L	R^2
RGO	4.63	0.0973	0.9859
RGO@Fe$_3$O$_4$	8.33	0.0647	0.9927

Conclusions

In conclusion, a reduced graphene oxide and Fe$_3$O$_4$ hybrid (RGO@Fe$_3$O$_4$) has been prepared for high performance capacitive deionization (CDI). The resultant Fe$_3$O$_4$ nanoparticle is fully encapsulated by RGO nanosheets and the specific surface area of RGO@Fe$_3$O$_4$ is 150.8 m^2/g. Cycle voltammetry curves indicate a typical electrical double layer capacitive behaviour and shows a higher specific capacity which is probably due to the hydroxylation of Fe$_3$O$_4$ surface. Compared to RGO, the electrosorption capacity and current efficiency of RGO@Fe$_3$O$_4$ is nearly two folds higher than that of RGO regardless of applied voltage. The kinetics and isotherm results also illustrate a higher electrosorption rate of RGO@Fe$_3$O$_4$ electrode. The maximum electrosorption capacity predicted from the Langmuir isotherm is 8.33 mg/g whereas the corresponding value for RGO is 4.63, indicating the great potential of RGO@Fe$_3$O$_4$ in application to CDI.

Acknowledgements

Notes and references

1   K. Laxman, M.T.Z. Myint, R. Khan, T. Pervez, J. Dutta, *Electrochimi. Acta*, 2015, **166**,329.
2   A. Subramani, J.G. Jacangelo, *Water Res.*, 2015, **75**, 164.
3   G.M. Geise, D.R. Paul, B.D. Freeman, *Prog. Polym. Sci.*, 2014, **39**, 1.
4   S. Porada, R. Zhao, A. van der Wal, V. Presser, P.M. Biesheuvel, *Prog. Mater. Sci*., 2013, **58**, 1388.
5   H.B. Li, Y. Gao, L.K. Pan, Y.P. Zhang, Y.W. Chen, Z. Sun, *Water Res*., 2008, **42**, 4923.
6   S. Porada, F. Schipper, M.Aslan, M. Antonietti, V.r Presser, Tim-Patrick Fellinger, *Chem. Sus. Chem*., 2015, **8**,1867.
7   Q. Dong, G. Wang, T.T. Wu, S.P. Peng, J.S Qiu, *J. Colloid Interface Sci.,* 2015, **446**, 373.
8   P. Xu, J.E. Drewes, D. Heil, G. Wang, *Water Res*., 2008, **42**, 2605.
9   H.B. Li, T. Lu, L.K. Pan, Y.P. Zhang, Z. Sun, *J. Mater. Chem*., 2009, **19**, 6773.
10 D.R. Dreyer, S.J. Park, C.W. Bielawski, R.S. Ruoff, *Chem. Soc. Rev*., 2010, **39**, 228.
11 D.S. Zhang, X.R. Wen, L.Y. Shi, T.T. Yan, J.P. Zhang,, *Nanoscale*, 2012, **4**, 5440.
12 H.B. Li, S. Liang, J. Li, L.J. He, *J. Mater. Chem. A*, 2013, **1**, 6335.
13 Z. Wang, B.J. Dou, L. Zheng, G. Zhang, Z.H. Liu, Z.P. Hao, *Desalination*, 2012, **299**, 96.
14 H. Wang, D.S. Zhang, T.T. Yan, X.R. Wen, J.P. Zhang, L.Y. Shi, *J. Mater. Chem. A*, 2013,**1**, 6335.
15 X.T. Xu, L.K. Pan, Y. Liu, T. Lu, Z. Sun, D.H.C. Chua, *Sci. Rep*., 2015, **5**, 8458
16 X.T. Xu, L.K. Pan, Y. Liu, T. Lu, Z. Sun, *J. Colloid Interface Sci.*, 2015, **445**, 143.
17 Y. Liu, X.T. Xu, T. Lu, Z. Sun, D.H.C. Chua, L.K. Pan, RSC Adv., 2015, **5**, 34117.
18 X.T. Xu, Y. Liu, T. Lu, Z. Sun, D.H.C. Chua, L.K. Pan, *J. Mater. Chem. A*, 2015,**3**, 13418.
19 H. Yin, H. Tang, D. Wang, Y. Gao, Z. Tang, *ACS Nano,* 2012, **6**, 8288.
20 Y. Zhao, C. Hu, Y. Hu, H. Cheng, G. Shi, L. Qu, *Angew. Chem. Int. Ed.* 2012, **124**, 11533
21 H. Wang, L.F. Cui, Y. Yang, H.S. Casalongue, J.T. Robinson, Y. Liang, Y. Cui, H. Dai, *J. Am. Chem. Soc.* 2010, **132**, 13978
22 K.C. Leonard, W.E. Suyama, M.A. Anderson, *Langmuir*, 2012 , **28**, 6476.
23 T.W. Lin, C.S. Dai, K.C. Hung, *Sci. Rep*., 2015, **4**, 7274.
24 H.B. Li, L.D. Zou, L.K. Pan, Z. Sun, *Environ. Sci. Technol.*, 2010, **44**, 8692.
25 H.B. Li, F. Zaviska, S. Liang, J. Li, L.J. He, H.Y. Yang, *J. Mater. Chem. A.*, 2014, **2**, 3484.
26 H.B. Li, L.K. Pan, C.Y. Nie, Y. Liu and Z. Sun, *J. Mater. Chem*., 2012, **22**, 15556.
27 H.J. Yin, S.L. Zhao, J.W. Wan, H.J. Tang, L. Chang, L.C. He, H.J. Zhao, Y. Gao, Z.Y. Tang, *Adv. Mater*. 2013, **25**, 6270.
28 H.X. Wu, T.J. Wang, Y. Jin, *Ind. Eng. Chem. Res.* 2007, **46**, 761.

RSC Advances Accepted Manuscript

163x80mm (150 x 150 DPI)